

Effect of ZnO on Structural and Magnetic Properties of MnFe₂O₄/ZnO Nanocomposite

B. Aslibeiki¹  · P. Kameli²

Received: 25 May 2015 / Accepted: 26 June 2015 / Published online: 25 July 2015
© Springer Science+Business Media New York 2015

Abstract In this paper, we reported a comparative study of structural and magnetic properties of MnFe₂O₄/ZnO nanocomposite and MnFe₂O₄ nanoparticles. The samples were prepared with a simple thermal decomposition method and then were characterized through thermogravimetry (TG) and differential thermal analysis (DTA), X-ray diffraction (XRD), field emission scanning electron microscope (FESEM) images, and vibrating sample magnetometry (VSM) at different temperatures. TG curves showed that pure samples can be obtained at 400 °C. XRD pattern of composite sample confirmed coexistence of crystalline cubic spinel Mn-ferrite and hexagonal zinc oxide phases. The estimated lattice parameter of MnFe₂O₄ nanoparticles, $a = 8.39 \text{ \AA}$, was smaller than bulk value ($a = 8.51 \text{ \AA}$) due to finite size effects. The magnetization of both samples followed the Bloch law with almost the same Bloch constant of $\beta \sim 5 \times 10^{-5} (\text{K}^{-3/2})$ showing similar spin wave excitation mechanisms in the samples. However, the VSM measurements indicated that increase of coercivity (H_c) of composite sample with decreasing the temperature is faster when compared with pure ferrite.

Keywords MnFe₂O₄/ZnO · Composite materials · Nanoparticles · Magnetization

1 Introduction

Ferrite/metal oxide nanocomposites have attracted research interest in the past few years because of their potential applications in different areas [1–6]. Blanco-Gutierrez et al. [1] studied the magnetic properties of MnFe₂O₄/SiO₂ (M: Co, Ni) nanocomposite. They compared the results with MnFe₂O₄ samples. They showed that the silica matrix avoids interaction between nanoparticles and modifies the magnetic properties of the composite samples. Winkler et al. [2] studied the origin of anisotropy in two different composite samples. They reported a coercivity of $H_c = 7.8 \text{ kOe}$ at 5 K for ZnO/CoFe₂O₄ core-shell nanoparticles. They showed that H_c can increase to a large value of 27.8 kOe for CoO/CoFe₂O₄ system. They claimed that the large anisotropy can be seen in the systems with non-magnetic (ZnO) or antiferromagnetic (CoO) core surrounded with a hard magnetic shell. Such a large coercivity makes these systems as good candidates for application in magnetic recording media. Sun et al. [5] studied the photocatalytic activity of ZnFe₂O₄/ZnO nanocomposites immobilized on graphene sheets. They reported that, ZnFe₂O₄ has a narrow band gap (1.9 eV) which favors the photocatalyst activity of composite sample under visible light irradiation. These studies show that ferrite/metal oxide nanocomposites can present better physical properties compared with pure ferrite nanoparticles.

Among spinel ferrites, the MnFe₂O₄ is a well-known material with interesting features such as simple and wide preparation methods, high chemical stability, low Curie temperature ($T_c \sim 580 \text{ K}$), and moderate saturation magnetization at 300 K ($M_s \sim 83 \text{ emu/g}$) [7]. Therefore, various studies on Mn-Ferrite nanoparticles properties have been reported in literature [8–16]. However there are few reports on MnFe₂O₄/metal oxide composite systems [17, 18]

✉ B. Aslibeiki
b.aslibeiki@tabrizu.ac.ir

¹ Department of Physics, University of Tabriz, Tabriz 51666-16471, Iran

² Department of Physics, Isfahan University of Technology, Isfahan, 84156-83111, Iran

In this study, $\text{MnFe}_2\text{O}_4/\text{ZnO}$ nanocomposite was prepared using a simple method, and the structural and magnetic properties of composite were compared with MnFe_2O_4 nanoparticles through different characterizations.

2 Experimental

$\text{MnFe}_2\text{O}_4/\text{ZnO}$ nanocomposite was synthesized using a thermal decomposition method based on the solidstate ball-milling and calcinations of nitrate precursors and citric acid [10]. The synthesis process is briefly summarized as follows: manganese nitrate ($\text{Mn}(\text{NO}_3)_2 \cdot 4\text{H}_2\text{O}$, Merck, 99 %), iron nitrate ($\text{Fe}(\text{NO}_3)_3 \cdot 9\text{H}_2\text{O}$, Merck, 99 %), and citric acid ($\text{C}_6\text{H}_6\text{O}_7$, Merck, 99.5 %) powders were mixed by an equal molar ratio of total metal nitrates to citric acid. The powders were ballmilled in a planetary ball mill for 1 h using agate balls. The ballmilled powders were annealed in an ambient air at 400°C , for 1 h to obtain MnFe_2O_4 nanoparticles. By annealing the obtained MnFe_2O_4 powder with zinc acetate ($\text{Zn}(\text{C}_2\text{H}_3\text{O}_2)_2 \cdot 2\text{H}_2\text{O}$, Merck, extra pure) and citric acid at 400°C for 1 h, $\text{MnFe}_2\text{O}_4/\text{ZnO}$ nanocomposite was obtained. The ZnO nanoparticle samples were synthesized according to the method of Zandi et al. [19]. In this method, zinc acetate and citric acid were mixed together and then ballmilled for 1 h. Then the ballmilled powders were annealed in an oven at 400°C for 2 h.

Thermogravimetry (TG) and simultaneous differential thermal analysis (DTA) of the initial precursors were recorded under air flow at a heating rate of $10^\circ\text{C}/\text{min}$ using a TG/DTA, BAHR STA 503 device. The crystalline structure of samples were analyzed, using a Philips X'Pert Pro MPD X-ray diffractometer with $\text{Cu-K}\alpha$ ($\lambda = 0.154$

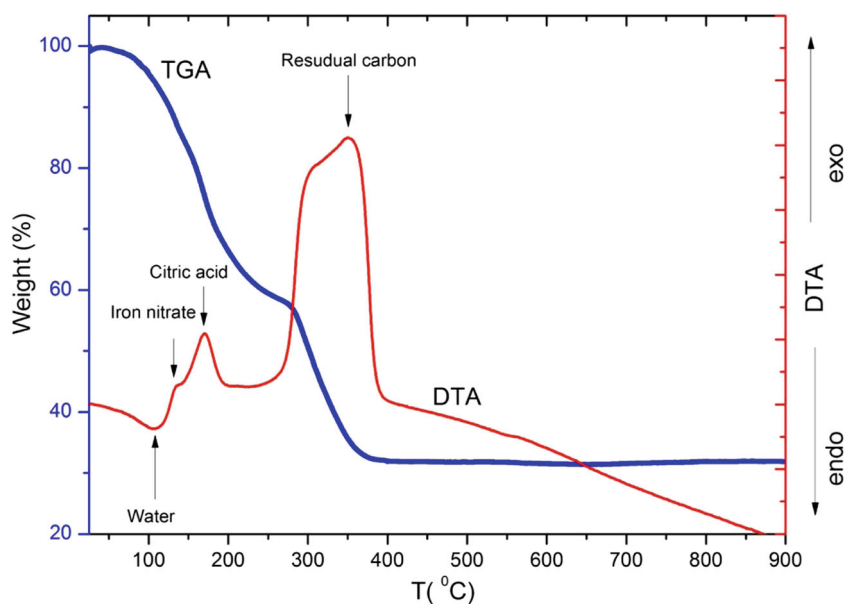
nm) radiation. Fourier transform infrared (FTIR) spectra of samples were recorded in a Tensor 27 spectrometer within the range of 400 to 4000 cm^{-1} . The microstructures and morphology of the samples was characterized by a TESCAN MIRA 3 field emission scanning electron microscope (FESEM) equipped with an energy dispersive X-ray spectrometer (EDXS). Magnetic measurements were performed by a vibrating sample magnetometer (VSM) with a maximum field of 20 kOe .

3 Results and Discussion

Figure 1 shows TG and DTA curves of metal nitrates and citric acid mixture. It can be seen from TG curve that, there are different weight loss regions which are further confirmed by simultaneous DTA curve. The endothermic peak around 100°C is due to water evaporation from the powders. With increasing the temperature, various losses in TG curve are observed. The weight losses accompanied with fluctuations in DTA curve at 135 , 170 , 307 , and 350°C are close to boiling point of manganese nitrate (100°C), iron nitrate (125°C), citric acid (175°C), and firing and removing of residual carbon form powders. It should be noted that because of the mixture nature of initial powders, the observed peaks could just be a sign of start point of thermally activated processes. As it is clear from the TG curve in Fig. 1, higher than 400°C , there is no noticeable weight variation of powders.

Figure 2 shows room temperature XRD pattern of samples. There is no noticeable trace of impurity phases in the XRD pattern of MnFe_2O_4 sample and the pattern confirms cubic spinel structure of the sample, comparable with the single-phase MnFe_2O_4 (card no. 73-1964). The composite

Fig. 1 TG and DTA curves of metal nitrates and citric acid mixture



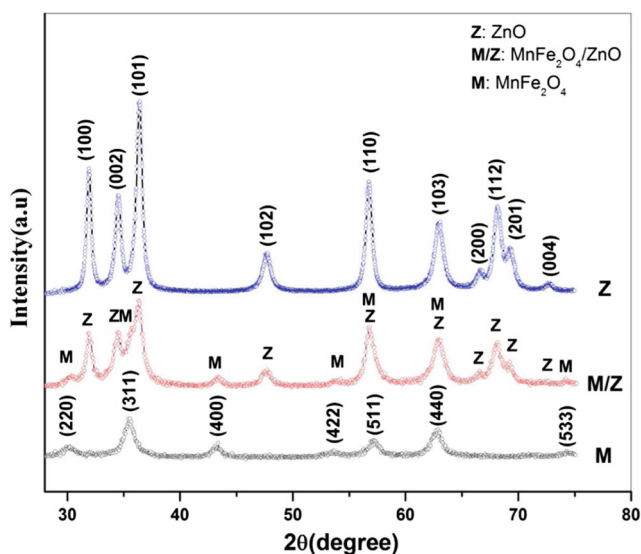


Fig. 2 X-ray diffraction patterns of the samples

sample consists of two crystalline phases. Bragg peaks of the XRD pattern of this sample are denoted by Z (for ZnO) and M (for spinel ferrite structure). The XRD pattern of ZnO confirms the formation of single hexagonal zinc oxide (card no. 36–1451).

The average crystallites size (*D*) of samples has been calculated according to Debye–Scherrer’s equation [20, 21]:

$$D = \frac{K\lambda}{\beta \cos \theta}, \tag{1}$$

Where *K* is the Scherrer’s constant (~ 0.9), λ is the wave length of the X-ray, β is the full-width at half maximum (FWHM) of the XRD peaks, and θ is the Bragg’s angle. The crystallite size of all the samples was obtained about 8 to 10 nm (see Table 1). The results suggested formation of single-domain particles in the powders.

Lattice constants (*a*, *c*) and volume of unit cell (*V*) were calculated using the lattice formula reported in ref. [20, 22], and the results are collected in Table 1.

Obtained *a* = 8.39 Å for MnFe₂O₄ nanoparticles is smaller than that for bulk manganese ferrite (8.51 Å) [7]. Similar results have been reported in literature [11, 23–25]. Finite size effects such as cation distribution and oxidation

Table 1 Crystallites size (*D*), lattice parameters (*a*, *c*), and volume of unit cell of samples

Sample	MnFe ₂ O ₄	MnFe ₂ O ₄ /ZnO	ZnO
<i>D</i> (nm)	8.7 (± 0.5)	9.9 (± 0.6)/8.3 (± 0.5)	10.3 (± 0.6)
<i>a</i> (Å)	8.39	8.34/3.23	3.23
<i>c</i> (Å)	–	–/5.20	5.19
<i>V</i> (Å ³)	591	580/47	47

of Mn²⁺ (0.81 Å) to Mn³⁺ (0.72 Å) can reduce the lattice parameter of ferrite nanoparticles [23, 26].

For composite sample, a smaller *a* = 8.34 Å than MnFe₂O₄ (*a* = 8.39 Å) was obtained. Slight replacement of Zn²⁺ (0.72 Å) ions in Mn²⁺ (0.81 Å) sites can reduce the lattice parameter. A similar result was reported for Zn-doped MnFe₂O₄ ferrite [27].

From Table 1, it can be seen that, the lattice parameters (*a*, *c*) of ZnO nanoparticles are identical for the composite and the ZnO sample. This result revealed that there is no intercalation of metal ions (Mn or Fe) in ZnO structure. In addition, the obtained lattice parameters for ZnO particles are in good accordance with literature [28–30].

Figure 3a–c illustrates the FESEM micrographs of the samples. Figure 3a shows that the ferrite sample consists of uniform particles (<20 nm). The ZnO sample in Fig. 3b consists of larger nanoaggregates with a size of <40 nm, because of larger particle size of ZnO nanoparticles than MnFe₂O₄ sample. The image of composite sample in Fig. 3c confirms mixed ferrite and ZnO nanoparticles with aggregate size between 20 and 40 nm.

Figure 3d shows the EDX spectrum of ferrite/ZnO composite. The spectrum confirmed the presence of Fe, Mn, and Zn elements in the sample with stoichiometric concentration.

The FTIR spectra of powder samples are shown in Fig. 4a. Broad peak centered at 3440 cm⁻¹ and the peak at 1640 cm⁻¹ correspond to the presence of stretching vibration O–H groups and residual H₂O molecules. The double peaks at 2920 and 2850 cm⁻¹ are related to the C–H symmetrical and asymmetrical stretching bonds. The absorption band around 1380–1420 cm⁻¹ is due to the presence of trapped NO₃⁻ in the samples. The peaks around 1540–1560 cm⁻¹ correspond to C=O bands. There is signature of two important bands below 1000 cm⁻¹ in the FTIR spectra. The peak around 435 cm⁻¹ corresponds to vibration of octahedral metal–oxygen (M–O) bonds and the peak at 549 cm⁻¹ is attributed to vibration of tetrahedral M–O bonds [31]. The presence of these peaks as a wellknown feature of the spinel ferrites confirms the formation of metal–oxygen bands in the tetrahedral and octahedral sublattices of MnFe₂O₄ nanoparticles.

For ZnO sample, the peak at 570 cm⁻¹ is attributed to Zn–O bands, which is slightly larger than those reported in literatures [19, 32]. This shift could be related to structural deficiency and broken bonds in the sample. Muthukumarana and Gopalakrishnan [33] reported the value of 544 cm⁻¹ for pure ZnO nanoparticles, which is in good accordance with our result.

As it can be seen from Fig. 4b there is a small shift in the peak position toward lower wavenumbers. This result suggested the formation of Zn–O–M (M=Mn and Fe) bands in the composite sample during annealing the ferrite powders

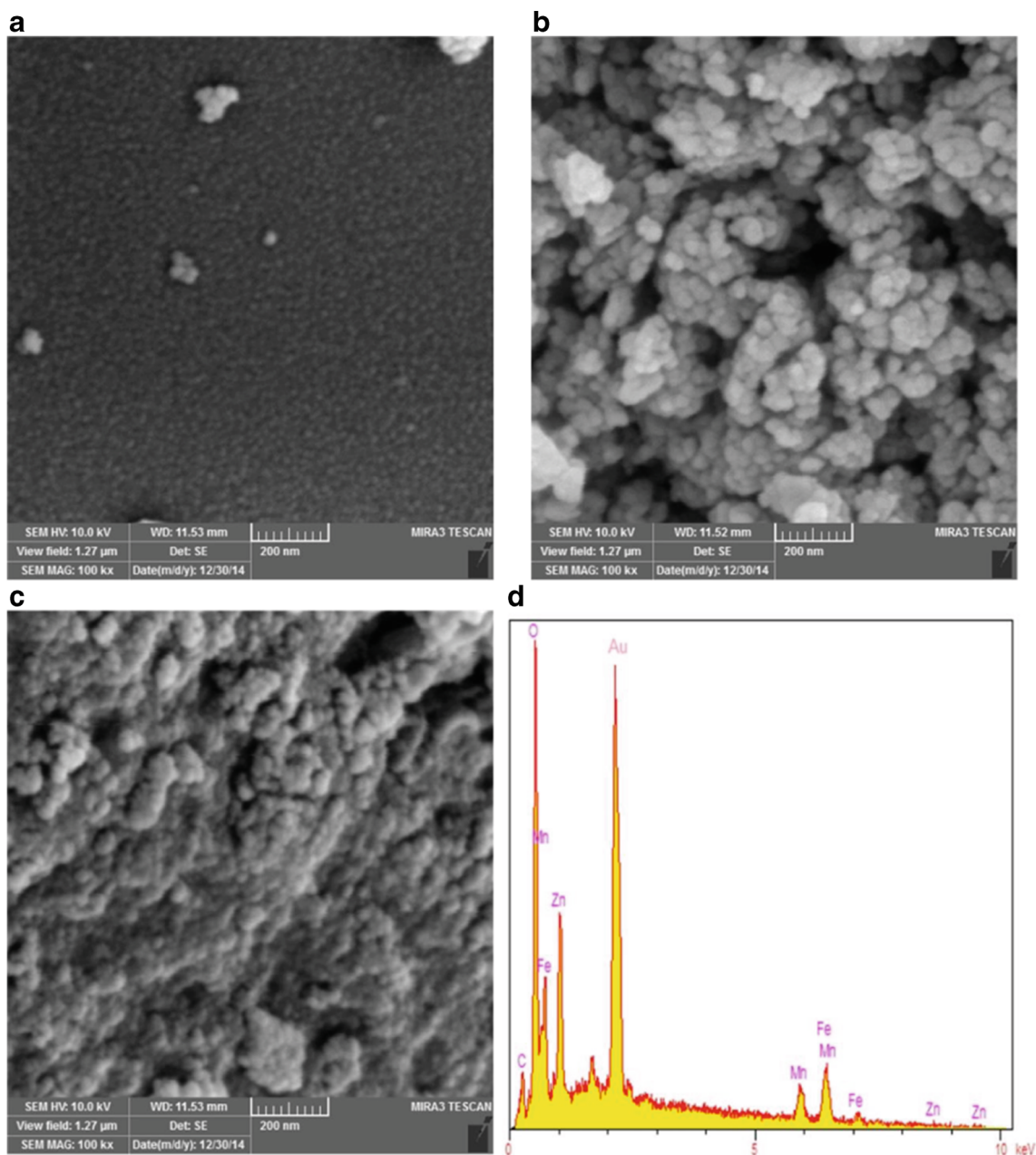


Fig. 3 FESEM images of **a** MnFe₂O₄, **b** MnFe₂O₄/ZnO, and **c** ZnO nanopowders. **d** EDX spectra of MnFe₂O₄/ZnO nanocomposite

with zinc acetate. This result was expected by considering the observed smaller lattice parameter of composite sample in comparison with MnFe₂O₄ sample.

3.1 Magnetic Properties

Figure 5a shows room temperature (300 K) magnetic hysteresis loops of the samples. As one can see from Fig. 5a, the coercivity (H_c) of ferrite and composite samples is almost zero and their particles are superparamagnetic at 300 K. The ZnO sample shows diamagnetic behavior with susceptibility

of -2.7×10^{-6} emu/g Oe, which is comparable with that reported in literature [28].

As temperature decreases, the thermal fluctuation energy cannot overcome the energy barrier between equilibrium states. Therefore, the number of blocked particles increases and the samples show non-zero coercivity and remanent magnetization (M_r). Figure 5b shows the hysteresis loops of samples at 120 K. From the inset in Fig. 5b, it is clear that all the samples have non-zero H_c and M_r at 120 K. Also the composite shows larger H_c (100 Oe) than MnFe₂O₄ sample (47 Oe). This result can be justified by larger particle size of

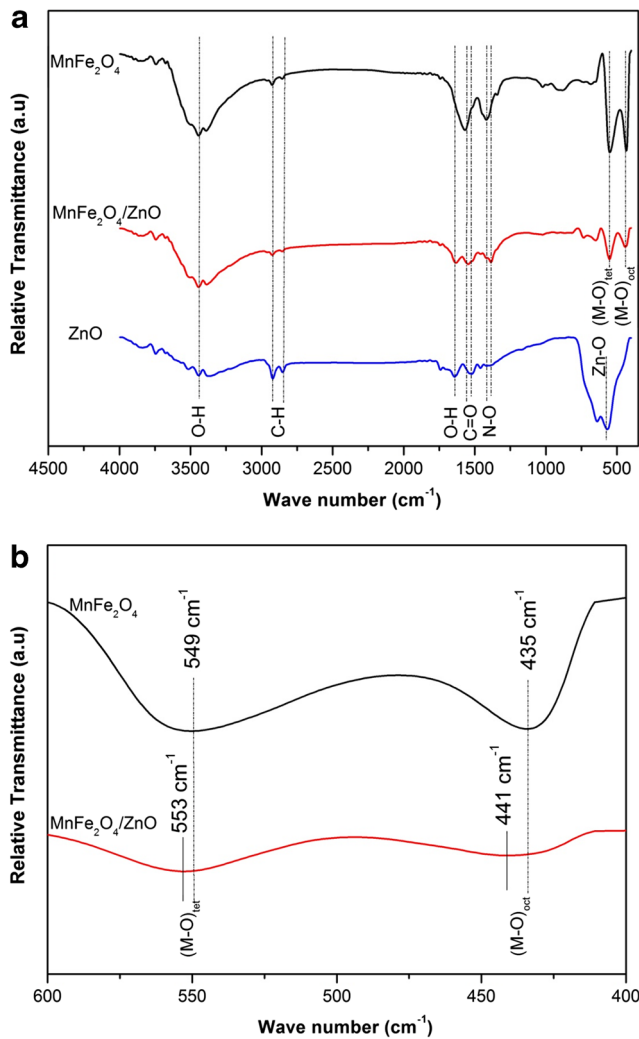


Fig. 4 FTIR spectra of the samples

composite than ferrite sample, as it was discussed in structural part. On the base of Néel model, the relaxation time of spin flip between equilibrium states is expressed as

$$\tau = \tau_0 \exp\left(\frac{E_a}{k_B T}\right) \tag{2}$$

Where τ_0 is in the range of 10^{-9} to 10^{-13} s. Energy barrier, E_a , is assumed to be proportional to particle volume V as $E_a = K_{\text{eff}}V$, where K_{eff} is an effective magnetic anisotropy constant. In the single-domain limit, with increasing the particles size and consequently increase of the energy barrier, larger thermal energy ($k_B T$) is needed to overcome the E_a . Below the blocking temperature, the remanent magnetization is non-zero and an external field (H_{ex}) should be applied to demagnetize the sample. At $H_{\text{ex}} = H_c$, the magnetization value returns to zero.

In addition to the particle size, slight replacement of Zn^{2+} ($m = 0 \mu_B$) ions in Mn^{2+} ($m = 5 \mu_B$) sites can increase the H_c of the system [34]. The Zn^{2+} ions prefer to

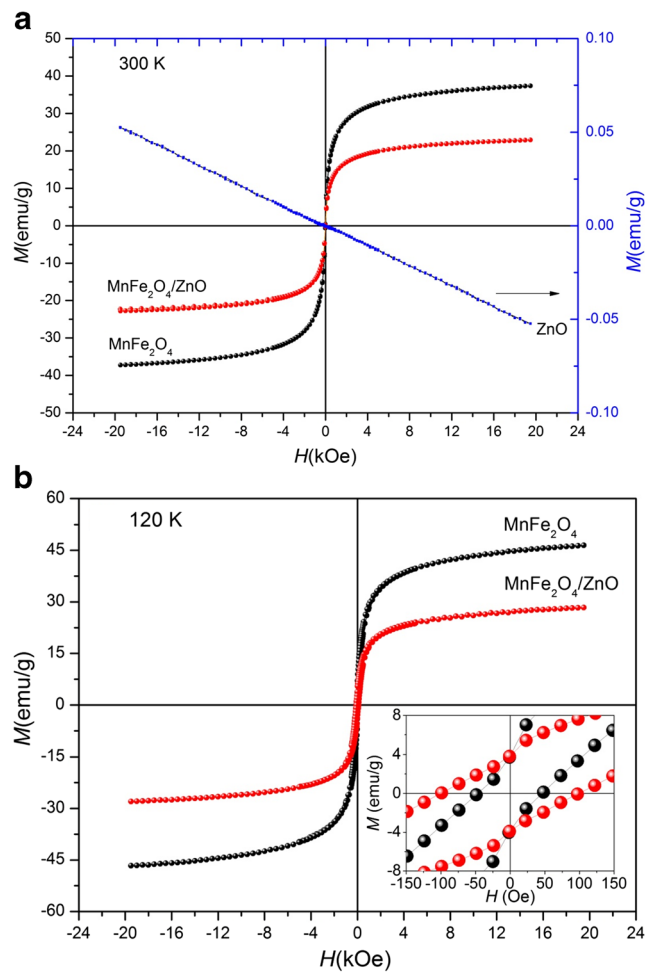


Fig. 5 Magnetic hysteresis loop of samples at a 300 K and b 120 K

substitute in tetrahedral sites of spinel structure, therefore increase the magnetization of sample [35, 36]. Increasing the magnetic moment of nanoparticles can alter the coercivity of the sample.

Figure 6a, b shows temperature dependence $M-H$ curves of the samples. Inset shows increase of M_r and H_c with decreasing the measurement temperature. Also, magnetization at 2 T (M_{2T}) increases as temperature decreases. The Bloch law has usually been used to study the temperature dependence behavior of saturation magnetization, $M_s(T)$ at intermediate temperatures :

$$M_s(T) = M_s(0)(1 - \beta T^{3/2}) \tag{3}$$

Where $M_s(0)$ is the saturation magnetization at absolute zero and β is called the Bloch constant. We used M_{2T} instead of M_s and then the data were fitted with (3). Figure 7a shows the best fits of data with (3). The obtained $\beta = 4.8 \times 10^{-5} (\text{K}^{-3/2})$ is in good accordance with that reported for MnFe_2O_4 nanoparticles [14, 37]. The $\beta = 5 \times 10^{-5} (\text{K}^{-3/2})$ of composite sample is comparable with that

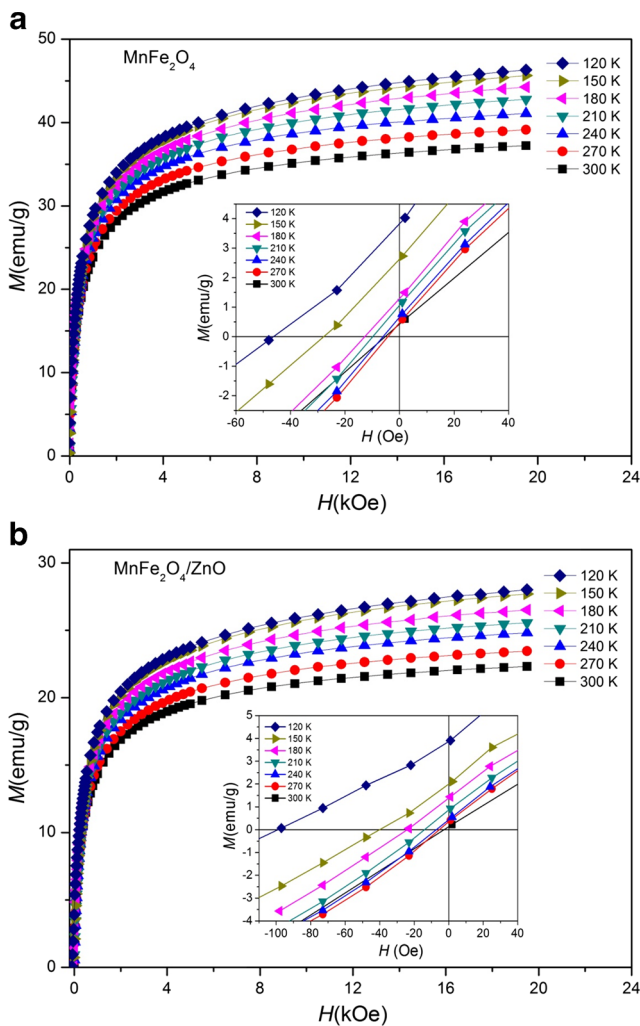


Fig. 6 M – H curves of samples at different temperatures

of pure ferrite sample, which confirms similar spin wave excitation in both the samples.

Figure 7b shows the variation of H_c with temperature. Kneller's law describes the temperature dependence coercivity of non-interacting nanoparticles below blocking temperature, T_B , as

$$H_C(T) = H_C(0) \left[1 - \left(\frac{T}{T_B} \right)^{1/2} \right] \quad (4)$$

Where $T_B = KV/25k_B$ and $H_C(0) = 2K/M_s$ is the coercivity of uniaxial particles at absolute zero [38]. We tried to fit the experimental data with (4). The obtained fit results were not successful (not shown here). Shendurk et al. [39] observed the same results when they examined the coercivity of γ - Fe_2O_3 nanoparticles with Kneller's law. They justified their result by considering the temperature dependence anisotropy constant, K_{eff} , and surface effects.

Yoon and Krishnan [40] showed that, at low temperatures ($T < 100$ K), the K_{eff} of $MnFe_2O_4$ nanoparticles is strongly

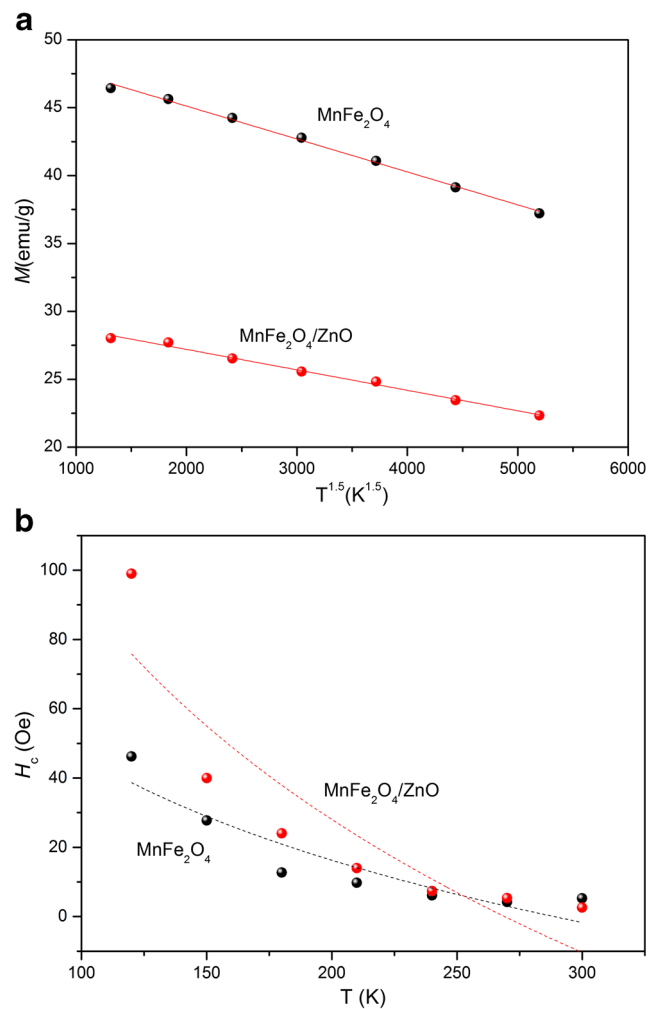


Fig. 7 **a** Temperature dependence behavior of M_{2T} fitted by Bloch equation. **b** Coercivity, H_c , of samples at different temperatures. The dashed lines show the fit result of modified Kneller's law

temperature dependent. They reported a large increase in K_{eff} with decreasing the temperature. At low temperatures, the surface anisotropy has important contribution to the K_{eff} value [39]. On the other hand, the K_{eff} of $MnFe_2O_4$ nanoparticles remains almost constant at higher than 100 K [40], which is our case. We observed a strongly interacting superspin glass state (SSG) in $MnFe_2O_4$ nanoparticles [41]. Therefore, deviation from Kneller's law could be due to the presence of unblocked particles and also interparticle interactions in the samples.

For a system of interacting particles, the modified Kneller's law is given as

$$H_C(T) = H_C(0) \left[1 - \left(\frac{T}{T_B} \right)^\alpha \right] \quad (5)$$

In which the exponent α depends on interaction strength and particle size distribution. If the exchange interactions are dominant, H_c increases with interaction strength. On the

other hand, the dipole–dipole interactions reduce the H_c [42, 43]. Therefore, two different regions are expected. The $0 < \alpha < 0.5$ for dipole–dipole interactions and $0.5 < \alpha < 1$ if exchange interactions are dominant. Also, because of temperature dependence of surface effects, (5) could not be applied for the entire temperature interval.

Peddis et al. [44] reported the value of $\alpha = 3/4$ for $\delta-(\text{Fe}_{0.67}\text{Mn}_{0.33})\text{OOH}$ nanoparticles in temperatures 5 to 150 K. However, the fit results for our samples were not reasonable in any temperature interval. Manova et al. [45] observed an exponential decay in H_c of CoFe_2O_4 nanoparticles with increasing the temperature. It seems that, an exponential function can well describe the temperature dependence behavior of H_c of present samples.

Another interesting result was the different temperature dependence behavior between H_c of composite and the pure MnFe_2O_4 sample. The H_c at 300 K shows very small values of 5 and 3 Oe for MnFe_2O_4 and composite samples, respectively, which suggested the presence of SPM particles in both the samples. At 120 K, the H_c raised to 46 and 99 Oe for MnFe_2O_4 and composite samples, respectively. Although both the samples show $H_c \sim 0$ at room temperature, the H_c of composite is two times larger than ferrite sample at 120 K. Such an increase in H_c of composite sample could be due to the presence of Zn–O–Mn and Zn–O–Fe bond in the surface, in addition to slightly larger particles of composite than pure ferrite sample.

4 Conclusions

In this work, an easy synthesis route of $\text{MnFe}_2\text{O}_4/\text{ZnO}$ nanocomposite has been presented. The structural and magnetic properties of nanocomposite have been compared with pure MnFe_2O_4 nanoparticles. Results showed that both samples are superparamagnetic at room temperature. Below 300 K, the composite showed larger coercivity H_c compared with pure ferrite sample. An exponential-like decay was observed in H_c with increasing the temperature.

References

- Blanco-Gutiérrez, V., Virumbrales, M., Saez-Puche, R., Torralvo-Fernandez, M.J.: *J. Phys. Chem. C* **117**, 20927–20935 (2013)
- Winkler, E.L., Lima, J.E., Tobia, D., Saleta, M.E., Troiani, H.E., Agostinelli, E., Fiorani, D., Zysler, R.D.: *Appl. Phys. Lett.* **101**, 252405–252404 (2012)
- Wilson, A., Mishra, S.R., Gupta, R., Ghosh, K.: *J. Magn. Magn. Mater.* **324**, 2597–2601 (2012)
- Chen, W., Zheng, J., Li, Y.: *J. Alloys Compd.* **513**, 420–424 (2012)
- Sun, L., Shao, R., Tang, L., Chen, Z.: *J. Alloys Compd.* **564**, 55–62 (2013)
- Jiang, J., Ai, L.H.: *J. Mater. Sci.: Mater. Electron.* **21**, 687–691 (2010)
- Goldman, A.: *Modern ferrite technology*. Springer, New York (2005)
- Günay, M., Erdemi, H., Baykal, A., Sözeri, H., Toprak, M.S.: *Mater. Res. Bull.* **48**, 1057–1064 (2013)
- Aslibeiki, B., Kameli, P.: *J. Magn. Magn. Mater.* **385**, 308–312 (2015)
- Aslibeiki, B., Kameli, P., Salamati, H.: *J. Magn. Magn. Mater.* **324**, 154–160 (2012)
- Akhtar, M., Younas, M.: *Solid State Sci.* **14**, 1536–1542 (2012)
- Li, J., Yuan, H., Li, G., Liu, Y., Leng, J.: *J. Magn. Magn. Mater.* **322**, 3396–3400 (2010)
- Balaji, G., Gajbhiye, N.S., Wilde, G., Weissmüller, J.: *J. Magn. Magn. Mater.* **242–245, Part 1**, 617–620 (2002)
- Chen, J., Sorensen, C., Klabunde, K., Hadjipanayis, G., Devlin, E., Kostikas, A.: *Phys. Rev. B* **54**, 9288 (1996)
- Tang, Z.X., Sorensen, C.M., Klabunde, K.J., Hadjipanayis, G.C.: *Phys. Rev. Lett.* **67**, 3602–3605 (1991)
- Lin, X., Lv, X., Wang, L., Zhang, F., Duan, L.: *Mater. Res. Bull.* **48**, 2511–2516 (2013)
- Takamura, H., Sugai, H., Watanabe, M., Kasahara, T., Kamegawa, A., Okada, M.: *J. Electroceram.* **17**, 741–748 (2006)
- Xiao, H.-M., Liu, X.-M., Fu, S.-Y.: *Compos. Sci. Technol.* **66**, 2003–2008 (2006)
- Zandi, S., Kameli, P., Salamati, H., Ahmadvand, H., Hakimi, M.: *Phys. B Condens. Matter* **406**, 3215–3218 (2011)
- Aslibeiki, B., Kameli, P., Salamati, H.: *J. Nanoparticle Res.* **15**, 1–12 (2013)
- Cullity, B.D., Stock, S.R.: *Elements of X-ray Diffraction*, Prentice hall Upper Saddle River (2001)
- Akther Hossain, A., Tabata, H., Kawai, T.: *J. Magn. Magn. Mater.* **320**, 1157–1162 (2008)
- Yang, A., Chinnasamy, C.N., Greneche, J.M., Chen, Y., Yoon, S.D., Hsu, K., Vittoria, C., Harris, V.G.: *Appl. Phys. Lett.* **94**, 113109–113103 (2009)
- Yang, A., Chinnasamy, C., Greneche, J., Chen, Y., Yoon, S.D., Hsu, K., Vittoria, C., Harris, V.: *Appl. Phys. Lett.* **94**, 113109 (2009)
- Chinnasamy, C., Yang, A., Yoon, S., Hsu, K., Shultz, M., Carpenter, E., Mukerjee, S., Vittoria, C., Harris, V.: *J. Appl. Phys.* **101**, 09M509 (2007)
- van der Zaag, P.J., Brabers, V.A.M., Johnson, M.T., Noordermeer, A., Bongers, P.F.: *Phys. Rev. B* **51**, 12009–12011 (1995)
- Varshney, D., Verma, K., Kumar, A.: *Mater. Chem. Phys.* **131**, 413–419 (2011)
- He, M., Tian, Y., Springer, D., Putra, I., Xing, G., Chia, E., Cheong, S., Wu, T.: *Appl. Phys. Lett.* **99**, 222511 (2011)
- Liu, Z., Liu, Y., Yao, K., Ding, Z., Tao, J., Wang, X.: *J. Mater. Synth. Process.* **10**, 83–87 (2002)
- Zhao, L., Zhang, H., Zhou, L., Xing, Y., Song, S., Lei, Y.: *Chem. Commun.*, 3570–3572 (2008)
- Aslibeiki, B.: *Curr. Appl. Phys.* **14**, 1659–1664 (2014)
- Cao, X., Meng, J., Mi, F., Zhang, Z., Sun, J.: *Solid State Commun.* **151**, 678–682 (2011)
- Muthukumar, S., Gopalakrishnan, R.: *Opt. Mater.* **34**, 1946–1953 (2012)
- Hou, X., Feng, J., Liu, X., Ren, Y., Fan, Z., Zhang, M.: *J. Colloid Interface Sci.* **353**, 524–529 (2011)
- Kondo, T., Mori, K., Hachisu, M., Yamazaki, T., Okamoto, D., Watanabe, M., Gonda, K., Tada, H., Hamada, Y., Takano, M., Ohuchi, N., Ichianagi, Y.: *J. Appl. Phys.* **117**, 17D157 (2015)
- Arulmurugan, R., Vaidyanathan, G., Sendhilnathan, S., Jeyadevan, B.: *J. Magn. Magn. Mater.* **298**, 83–94 (2006)

37. Aquino, R., Depeyrot, J., Sousa, M.H., Tourinho, F.A., Dubois, E., Perzynski, R.: *Phys. Rev. B* **72**, 184435 (2005)
38. Mohapatra, J., Nigam, S., Gupta, J., Mitra, A., Aslam, M., Bahadur, D.: *RSC Advances* **5**, 14311–14321 (2015)
39. Shendruk, T., Desautels, R., Southern, B., Van Lierop, J.: *Nanotechnology* **18**, 455704 (2007)
40. Yoon, S., Krishnan, K.M.: *J. Appl. Phys.* **109**, 07B534–533 (2011)
41. Aslibeiki, B., Kameli, P., Salamati, H., Eshraghi, M., Tahmasebi, T.: *J. Magn. Magn. Mater.* **322**, 2929–2934 (2010)
42. Vargas, J.M., Nunes, W.C., Socolovsky, L.M., Knobel, M., Zanchet, D.: *Phys. Rev. B* **72**, 184428 (2005)
43. Kechrakos, D., Trohidou, K.: *Phys. Rev. B* **58**, 12169 (1998)
44. Peddis, D., Rinaldi, D., Ennas, G., Scano, A., Agostinelli, E., Fiorani, D.: *Phys. Chem. Chem. Phys.* **14**, 3162–3169 (2012)
45. Manova, E., Kunev, B., Paneva, D., Mitov, I., Petrov, L., Estournès, C., D'Orléan, C., Rehspringer, J.-L., Kurmoo, M.: *Chem. Mater.* **16**, 5689–5696 (2004)